Journal of Magnetism and Magnetic Materials 335 (2013) 75–85

Contents lists available at SciVerse ScienceDirect

Journal of Magnetism and Magnetic Materials

journal homepage: www.elsevier.com/locate/jmmm

Microstructure and magnetic properties of as-cast Ni_2MnGa alloys processed by twin roller melt spinning

G. Pozo López [a,b,*], A.M. Condó [c,d,e], R.N. Giordano [a], S.E. Urreta [a], N. Haberkorn [c,e], E. Winkler [c,d,e], L.M. Fabietti [a,b]

[a] Facultad de Matemática, Astronomía y Física, Universidad Nacional de Córdoba, Ciudad Universitaria, 5000 Córdoba, Argentina
[b] Instituto de Física Enrique Gaviola – CONICET, Argentina
[c] Centro Atómico Bariloche, Comisión Nacional de Energía Atómica. Av. Bustillo 9500, 8400 San Carlos de Bariloche, Argentina
[d] Instituto Balseiro, Universidad Nacional de Cuyo. Av. Bustillo 9500, 8400, San Carlos de Bariloche, Argentina
[e] Consejo Nacional de Investigaciones Científicas y Técnicas (CONICET), Argentina

ARTICLE INFO

Article history:
Received 25 November 2012
Received in revised form
26 January 2013
Available online 9 February 2013

Keywords:
Ni_2MnGa alloy
Twin roller melt spinning
Shape memory
X-ray diffraction
TEM
Magnetic property

ABSTRACT

The magnetism and the microstructure of Ni_2MnGa alloys, processed for the first time by twin roller melt spinning at tangential wheel speeds of 10 m/s (V10), 15 m/s (V15) and 20 m/s (V20) are investigated. At room temperature, the major phase in the as-cast alloys is the cubic $L2_1$ Ni_2MnGa ordered austenitic phase, with a lattice parameter only ~0.1% larger than the tabulated value. The order domain size in the austenitic phase decreases from (40 ± 1) nm in samples V10 to (19 ± 1) nm in V20. Mn(S,Se) small precipitates are also found uniformly embedded in the ribbons with mean size of (26 ± 2) nm (V10) and (7 ± 2) nm (V20), exhibiting a definite orientation relation with the austenitic matrix, $<1\,0\,0>_P // <1\,0\,0>_a$. The as-cast alloys transform to an intermediate cubic phase I at about 220–230 K depending on the quenching rate and to a martensitic phase at about 130 K. The high temperature austenitic phase and the low temperature martensitic phase are ferromagnetic; in both cases the saturation polarization is lower in samples quenched at higher rates. The demagnetization curves measured from saturation in the martensitic state show two marked steps: a first one for positive fields in V15 and V10 (~46 mT) and a larger second one for relatively large inverse fields (~130–250 mT) in all the samples. These steps are likely to arise from a demagnetization mechanism involving a field induced twin boundary motion in the few martensite variants selected by the crystallographic texture and the quenched stresses in the ribbons.

1. Introduction

Ferromagnetic shape memory alloys are active materials which may undergo relatively large strains by the motion of twin boundaries in a magnetic martensitic phase. In Ni_2MnGa alloys, this phenomenon leading to large magnetic field-induced strains (MFIS) was first reported by Ullakko et al. in 1996 [1]. More recently, strains of about 9.5% were induced by a magnetic field below 1 T in unstressed single crystals of the NiMnGa orthorhombic seven-layered martensitic phase [2].

Upon cooling from the melt, the Ni_2MnGa alloy undergoes multiple phase transformations: an ordering transition (B2 to $L2_1$), a ferromagnetic phase transformation and also a structural martensitic transformation [3]. In this alloy, the martensitic transition temperature is lower than the Curie point and any composition change makes these characteristic temperatures approach each other.

These magnetic shape memory materials have a high potential in the design of fast actuating devices and sensors [4,5] and they have been largely investigated both, theoretically and experimentally [6–11]. The magnetic-field-induced strain is due to twin boundaries moving under the influence of an internal stress produced by the magnetic anisotropy energy: in general, this strain is not recovered upon field removal [12,13] as observed with the true plastic strain produced by twin boundary motion induced by an externally applied stress in nonmagnetic shape-memory alloys.

In polycrystalline magnetic shape memory alloys, these magnetoplastic strains solely produced by magnetic forces at constant temperature, with no mechanical bias stress, are negligibly small as compared to those found in single crystals. In other words, when the field is removed, the variants do not reorient themselves back in their original orientation but a compressive bias stress must be

* Corresponding author at: Facultad de Matemática, Astronomía y Física, Universidad Nacional de Córdoba, Ciudad Universitaria, 5000 Córdoba, Argentina. Tel.: +54 351 4334051; fax: +54 351 4334054.
E-mail address: gpozo@famaf.unc.edu.ar (G. Pozo López).

0304-8853/$ - see front matter © 2013 Elsevier B.V. All rights reserved.
http://dx.doi.org/10.1016/j.jmmm.2013.01.040

applied perpendicular to the field direction to reorient the field-induced variants back and hence achieve reversible MFIS.

For applications in miniature actuators and to minimize the ac eddy-current losses, some attempts have been made to process the alloy as thin films [14–16], particles [17,18] and ribbons [19–23]. In this sense, melt spinning is an effective way to produce textured polycrystalline ribbons of FSMAs [19,21,22,24,25]. Compared to the as-cast master alloy, the as-quenched ribbons exhibit a lower martensitic transformation temperature T_M and Curie temperature T_C, and a reduced saturation magnetization M_S; these characteristic parameters further decrease in samples processed at higher spinning rates [26]. The melt spun polycrystalline Ni–Mn–Ga ribbons exhibit in the as-cast condition, and even after annealing at temperatures below 773 K, a marked step in the $M(H)$ hysteresis loops [25], which has been attributed to magnetic field induced twin boundary motion (MFITBM), in the particular scenario of quenched-in internal stresses, built up during solidification onto the rotating copper wheel.

This article reports on the magnetism and the microstructure of Ni_2MnGa alloys, processed for the first time in a twin roller melt spinning device: this technique is known to impose a symmetric heat extraction during solidification, leading to high quenched-in stresses and an enhanced crystalline texture, as compared to conventional (single wheel) melt spinning. Different tangential wheel speeds were applied to obtain ribbons cooled at different rates.

2. Experimental procedures

A master alloy of nominal composition Ni_2MnGa was prepared by arc melting 99.9% Ni (Strem Chemicals), 99.95% Mn (Alfa Aesar) and 99.99% Ga (Strem Chemicals); the small ingots so obtained (about 5 g) were further re-melted four times to promote an homogeneous distribution of the components. All these procedures were conducted under a Zr gettered Ar atmosphere. The weight loss in the different ingots during arc melting was found to be less than 0.3%. The alloy was further processed in a twin roller melt spinning device at three different tangential wheel speeds: 10 m/s, 15 m/s and 20 m/s to obtain samples V10, V15 and V20, respectively. The springs forcing the contact between the two rolling wheels were set to 24 N. The alloy was obtained as ribbons of about 1.1–1.9 mm wide and 44–45 μm thick, as shown in Table 1. Ribbons morphology was examined in a Leica DMRM optical microscope. No differences between the ribbon faces could be observed – see Fig. 1 – indicating symmetric solidification conditions.

The resulting microstructures were characterized by X-ray diffraction (XRD), scanning electron microscopy (SEM) and transmission electron microscopy (TEM). X-ray diffraction profiles were recorded in a Philips PW 1710/01 diffractometer in the 2θ range from 20° to 100°, in Bragg-Brentano configuration, using Cu Kα radiation ($\lambda = 1.5418$ Å) and a graphite monochromator. Samples

Table 1
Mean thickness t and width w of the ribbons V10, V15 and V20. Lattice constant a_a, mean lattice strain e and intensity ratios (I_{400}/I_{220}) of the high temperature austenitic phase, obtained from XRD data, are also listed. Card ICSD #103803 indicates $a_0 = 5.825$ Å at room temperature and (I_{400}/I_{220})= 0.15.

Sample	V10	V15	V20
w [mm]	1.9 ± 0.4	1.4 ± 0.2	1.1 ± 0.2
t [μm]	45 ± 3	44 ± 2	44 ± 2
a_a [Å]	5.832 ± 0.001	5.832 ± 0.001	5.834 ± 0.001
e ($\times 10^{-3}$)	0.22 ± 0.01	0.30 ± 0.01	0.35 ± 0.01
(I_{400}/I_{220})	0.25	0.34	0.52

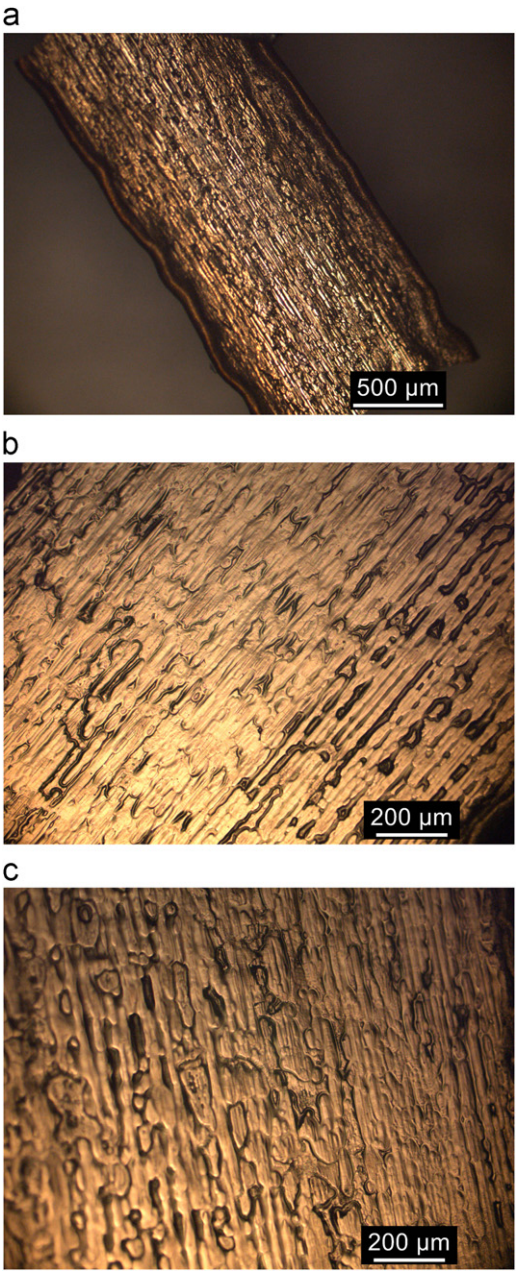

Fig. 1. Optical micrographs showing a typical ribbon quenched at 15 m/s (a), and two faces of a ribbon quenched at 10 m/s with quite similar morphologies (b), (c), indicating that they both solidified in contact with the mobile substrate.

observed by TEM were thin foils prepared by twinjet electropolishing with a 20% HNO_3 (nitric acid)/80% pro-analysis methanol electrolyte, at 12 V and 256 K. Transmission electron microscopy observations and selected area diffraction patterns were performed in a Philips CM 200 UT microscope, operating at 200 kV and equipped with energy-dispersive X-ray spectroscopy (EDS) facility. A FEI Nova NanoSEM 230 was used to image the ribbon fracture surfaces.

Magnetic measurements were performed in 6 mm long as-cast ribbons with the applied field parallel to the sample length. The demagnetizing factors N, calculated with the formalism proposed by [27] and using the software provided by [28], resulted in 0.016 ± 0.002 (V10), 0.013 ± 0.002 (V15) and 0.012 ± 0.002 (V20), respectively, leading to internal fields quite similar to the applied field. To calculate the magnetic polarization, a mean density of 8.134 g/cm^3 [29] was considered. Room temperature magnetic

hysteresis loops were measured in a vibrating sample magnetometer (VSM) Lakeshore 7300, with a maximum field up to 1.5 T. The magnetic polarization as a function of field and temperature was measured in a Quantum Design SQUID magnetometer, under an applied field of 2 mT (20 Oe) in the temperature range of 5–300 K. Curie temperatures were estimated from magnetization vs. temperature curves measured in a Faraday balance, in the 300–400 K temperature range.

Additionally, electrical transport was measured with the conventional four-probe geometry between room temperature and 20 K.

3. Results and discussion

3.1. X-ray diffraction analysis

The room temperature XRD patterns of the as-cast alloys, solidified at different rates, are shown in Fig. 2. The major phase is the cubic $L2_1$ Ni_2MnGa ordered austenitic phase in all the samples, as structure and order reflections are clearly identified [30]. In samples V15 two unidentified small peaks are also observed, indicated by "?" in Fig. 2b, which disappear after the sample is thinned a few microns, suggesting that they arise from a minor superficial phase. The mean crystallite size of this unknown phase is estimated using the Scherrer formulae [31,32] to be about 25 nm. The letter "T" in Fig. 2b denotes the diffraction peak of the double-coated tape used to paste the ribbons to the XRD specimen holder.

XRD patterns in Fig. 2a also indicate that the as-spun ribbons have some preferential orientation of the [4 0 0] direction perpendicular to the ribbon plane, which becomes more marked as the quenching rate increases, since the relative intensity (I_{400}/I_{220}), with a value of 0.15 in the reference powder pattern (card ICSD #103803), reaches values of 0.25, 0.34 and 0.52 in samples

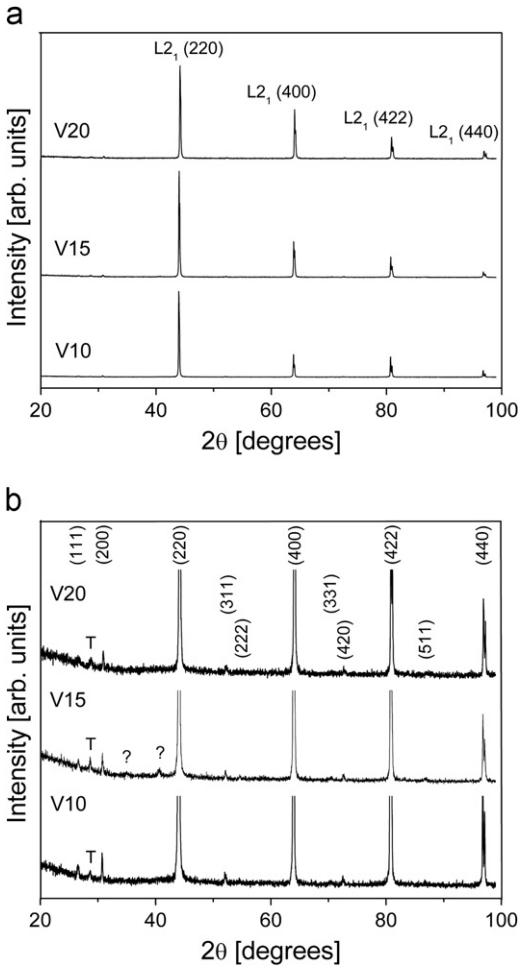

Fig. 2. (a) Room temperature X-ray diffraction patterns of the as-cast ribbons solidified at different wheels speeds. The relative intensities of the structural reflections from the ordered $L2_1$ cubic austenite structure can be observed. (b) Low intensity detail of a) showing fundamental and superlattice diffraction lines from $L2_1$ austenitic phase. Peaks indicated by "?" in sample V15 correspond to an unknown superficial phase while letter "T" denotes the diffraction peak of the double-coated tape used to paste the ribbons to the XRD specimen holder.

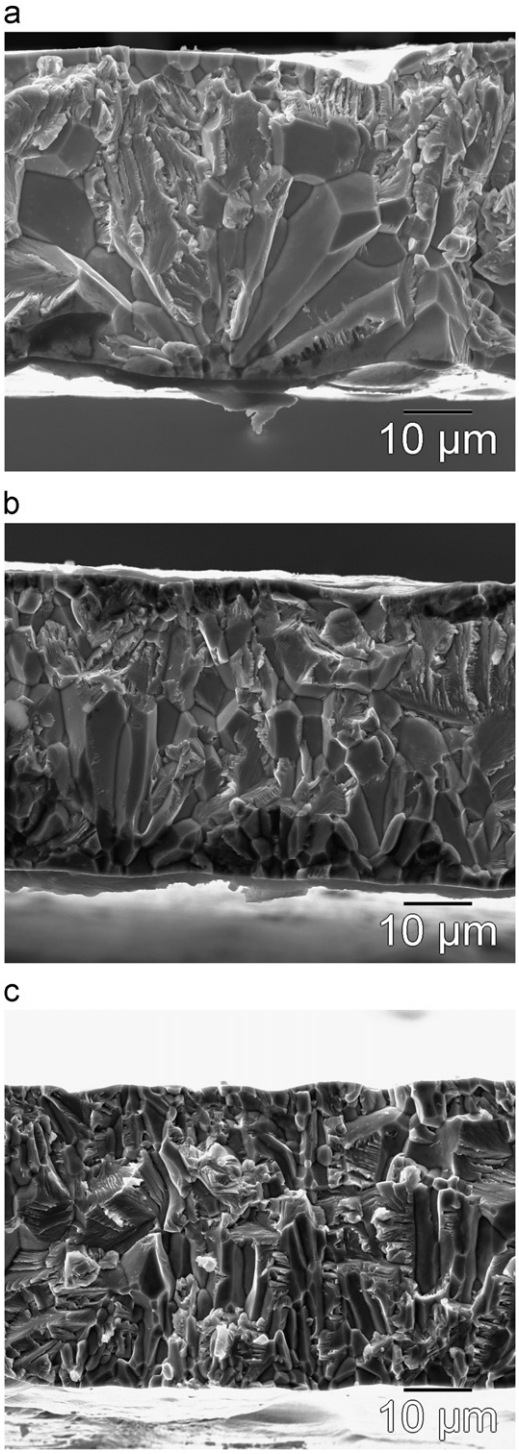

Fig. 3. SEM photographs imaged on the fractured cross section of ribbons (a) V10, (b) V15 and (c) V20.

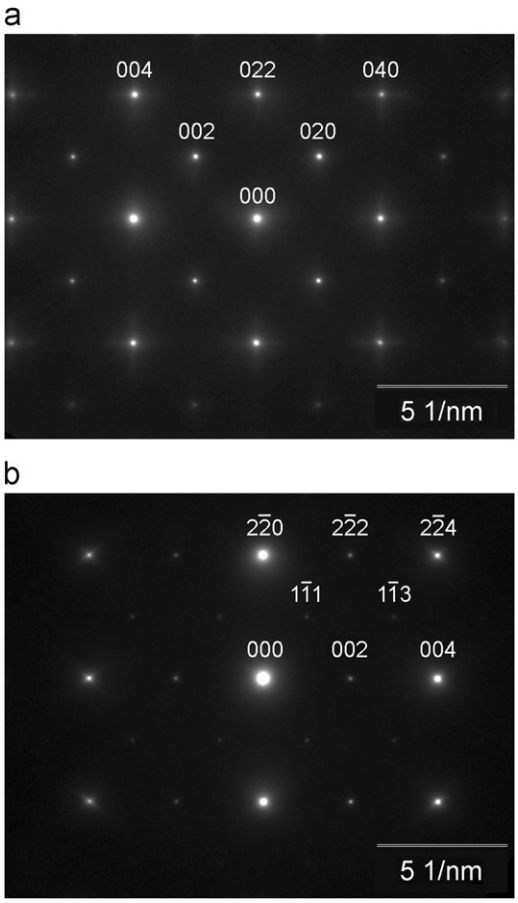

Fig. 4. Electron diffraction zone axis patterns from the austenite of sample V10 at room temperature corresponding to the $L2_1$ structure, (a) [1 0 0] and (b) [1 1 0].

V10, V15 and V20, respectively. This fact was already observed by Albertini and collaborators [21] in annealed single-roller melt-spun ribbons. In that case a change in the material texture during the heat treatment was observed: the (2 2 0) and (4 0 0) diffraction peaks roughly inverted their relative intensities on increasing the thermal treatment time.

The lattice constant a_a of the austenitic crystals was calculated by fitting to the structural reflections 220, 400, 422 and 440 a Pearson VII profile; corrected values of 2θ were used by considering the zero shift effect as described in [33]. The resulting values – listed in Table 1 – are indistinguishable within experimental errors; they coincide with the lattice parameter obtained by Ma et al. [34] and are only $\sim$0.1% larger than the value a_0=5.825 Å reported by Webster et al. [35] and tabulated in card ICSD #103803.

Approximate values for the mean lattice strain e were determined using the Stokes and Wilson relation [31,32]: $e=\beta/(4\tan\theta)$, from measurements of the integral breath β of the structure reflection lines after correcting for instrumental broadening. As can be observed in Table 1, the mean lattice strain of the austenitic phase increases with the quenching speed.

3.2. Scanning electron microscopy

Fig. 3 shows SEM images of the fractured cross sections of the ribbons. Equiaxed grains of about 4 μm are observed on both surfaces (both solidified in contact with the wheels), while columnar grains appear in the middle region of the ribbons. These columnar grains are about 2–6 μm wide and 10–20 μm long, depending on the wheel speed. For sample V10, wider and longer columnar grains are encountered.

3.3. Transmission electron microscopy

Composition analysis on the melt-spun ribbons using energy-dispersive X-ray spectroscopy (EDS) revealed similar compositions

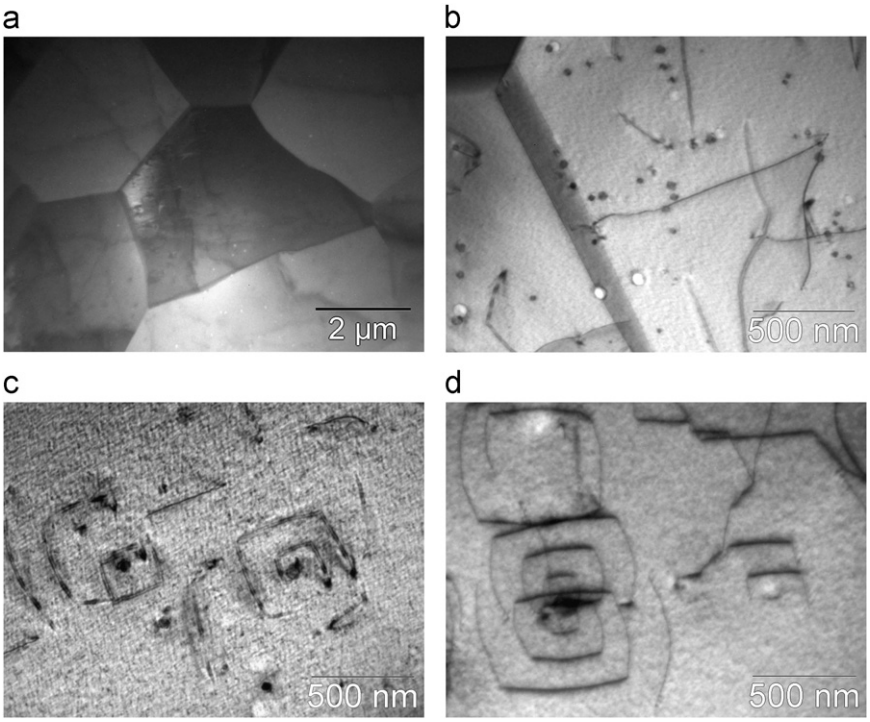

Fig. 5. TEM bright field micrographs showing (a) the general granular microstructure of the ribbons (V10), (b) the presence of precipitates and dislocations inside the grains (V10) and (c), (d) particular helical dislocation configurations around precipitates (V15 and V20 respectively).

in the three samples 50 at% Ni – 25 at% Mn – 25 at% Ga, with a quite narrow dispersion (less than 1 at%) around the nominal composition.

Conventional selected area electron diffraction (SAED) patterns confirmed the $L2_1$ crystalline structure of the austenite. Fig. 4 shows two zone axis diffraction patterns of the austenitic phase for sample V10 at room temperature. The [1 0 0] orientation (Fig. 4a) was mainly observed in accordance with XRD results. In the [1 1 0] orientation (Fig. 4b) the 111 and 113-type Heusler superlattice diffraction spots reveal the $L2_1$ atomic order in the ribbons. Similar results are obtained for the other samples, V15 and V20.

TEM bright field images reveal the polycrystalline morphology of the austenitic matrix, as shown in Fig. 5a, with mean grain sizes of about 2–5 μm in good agreement with previous SEM results. Additionally, dislocations and small precipitates are observed (Fig. 5b). Preferential etching around precipitates results in lighter circular regions or even holes which indicate that a precipitate was there. A detailed study about precipitates is presented in the following section. Particular dislocation configurations with helical shape were encountered around some precipitates, as can be seen in Fig. 5c, d. These dislocation configurations are similar to those already reported in quenched β-CuZnAlNi shape memory alloys with the same $L2_1$ structure [37] which were proposed to be the main vacancy sinks.

Dark field (DF) imaging using the 111 $L2_1$ superlattice reflection was performed to search for antiphase boundaries (APB) in very thin regions of the samples. Fig. 6a shows a typical dark field 111 image of the austenitic phase in sample V15, obtained from the [1 1 $\bar{2}$] zone axis SAED pattern in Fig. 6b. This zone axis is 35° away from a $<100>$-type direction and thus it was hardly achievable due to texture. The winding dark regions represent the APBs. The size of the order domains strongly depends on the quenching conditions; Fig. 6c–e shows the domain size histograms for the different samples and the corresponding fittings with a log-normal function, from which the mean domain diameter $<D_{APB}>$ and the distribution width, σ, were obtained. As can be seen, sample V20 presents the smallest antiphase domains and the narrowest size distribution.

3.4. Precipitates

As was already mentioned, small precipitates of a second phase were clearly observed by TEM. Fig. 7a shows a bright field image of the precipitates and its corresponding electron diffraction pattern close to a [1 1 $\bar{2}$] zone axis as in Fig. 6b. An additional reflection (P) from the precipitates close to the 222 diffraction spot can be observed. The dark field image with the reflection P can be observed in Fig. 7b. Comparing the bright and dark field images, it is evident that all the precipitates are diffracting indicating a definite orientation relationship with the matrix. The size of the precipitates was measured from the DF images. Fig. 7c, e summarizes the particle size histograms for the different samples and the corresponding log-normal distribution fittings, from which the mean precipitate diameter $<D_p>$ and the distribution width σ_p were obtained. Precipitate size is influenced by the quenching conditions; bigger precipitates are encountered for slowly cooled samples. Samples V20 present the smallest precipitates and the narrowest particle size distribution.

Fig. 8a shows a TEM bright field micrograph of a 70 nm diameter precipitate exhibiting Moiré fringes. In the upper side of the image, the corresponding electron diffraction pattern, again presents extra spots (P) corresponding to the precipitates. The nearness between the precipitate (P) and 022 austenitic matrix reflection produces the observed Moiré fringes in the precipitate (the ratio between the interplanar distances from precipitate and the matrix d_p/d_{a022} equals 0.910).

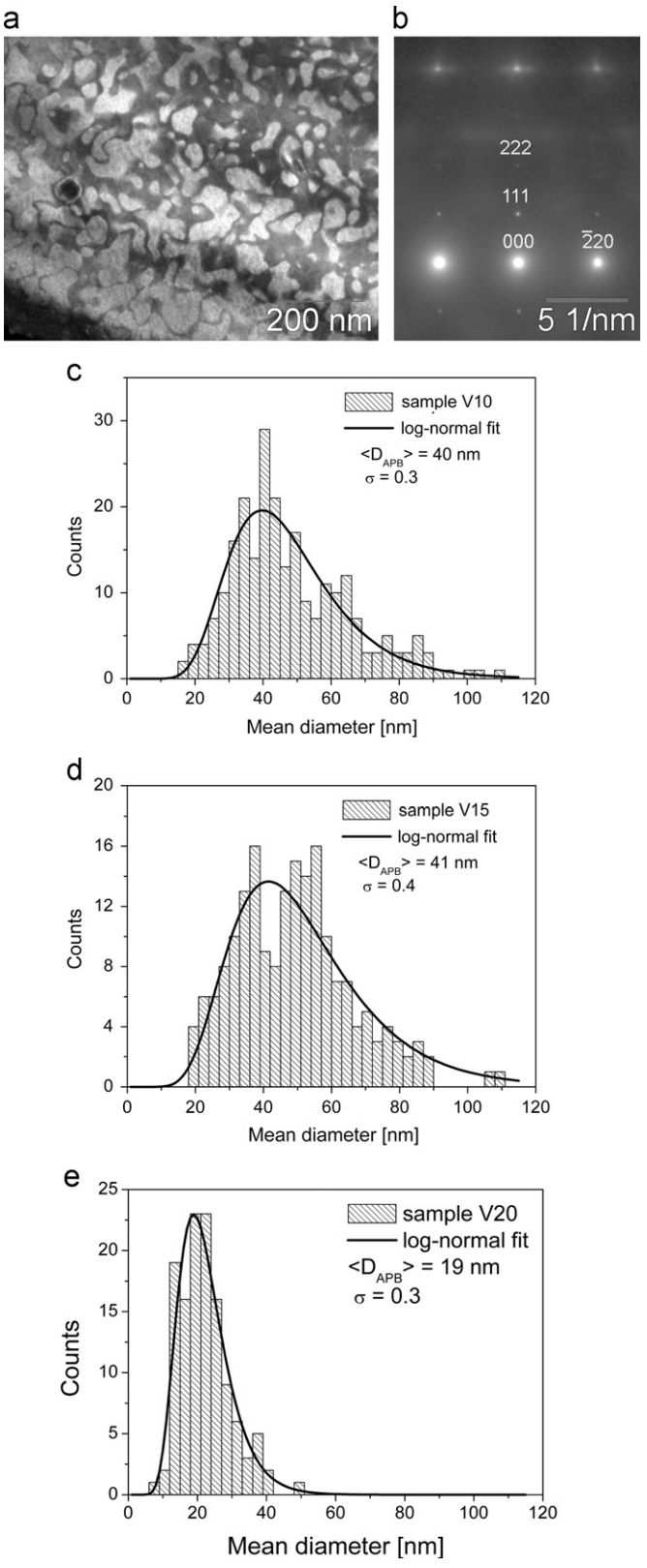

Fig. 6. (a) Typical view of the $L2_1$ antiphase boundaries in sample V15. (b) [1 1 $\bar{2}$] zone-axis electron diffraction pattern showing the 111 superlattice spot used for dark field imaging in (a). Antiphase boundary size histogram and its log-normal fitting for samples V10 (c), V15 (d) and V20 (e).

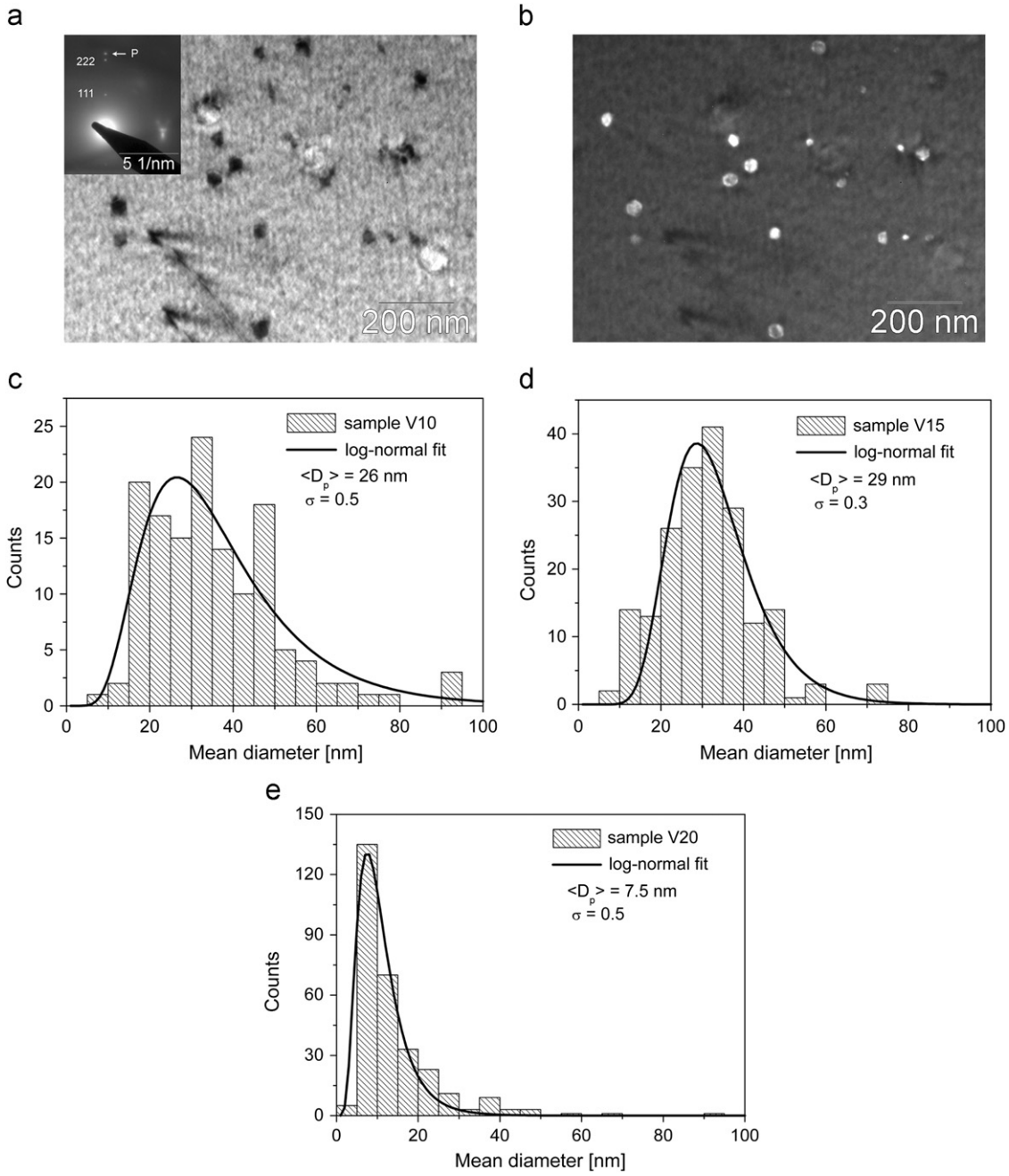

Fig. 7. (a) BF image from V15 sample showing precipitates close to the [1 1 $\bar{2}$] orientation. In the corresponding SAED pattern, shown in the inset, an additional reflection (P) corresponding to the precipitates is observed. (b) DF image with the reflection P reveals all the precipitates. Precipitate size histograms measured from the DF images of samples V10 (c), V15 (d) and V20 (e) together with its corresponding log-normal distribution fittings.

Fig. 8b presents a 110 nm diameter precipitate placed on the edge of a hole in the sample. Fine probe EDS microanalysis performed at each side of the precipitate/matrix interface evidence clear changes in composition: the precipitates are richer in Mn and poorer in Ga, and additionally contain Se and S. Selenium and sulfur are among two of the major impurities of the 99.95% Mn (Alfa Aesar) used in this work. Searching for possible compositions of the precipitates, we found that α-MnSe and α-MnS are stable compounds with NaCl-type structure with 5.440 Å and 5.224 Å lattice parameters respectively (slightly smaller than the lattice parameter of the austenite, Table 1).

A selected area electron diffraction pattern from a zone axis of the precipitate could be obtained (Fig. 8c) by tilting the sample. This pattern can be compared with the [1 1 1] zone axis pattern corresponding to α-MnSe (Fig. 8d). Since both patterns are similar, the experimental zone axis pattern obtained from the precipitates can be indexed as [1 1 1] of a Na–Cl-type structure with lattice parameter 5.309 Å. Considering this structure for the precipitates, the results in Figs. 7a and 8a can be expressed as $(222)_P//\ (222)_a$ and $(022)_P//\ (022)_a$. Therefore, the following orientation relation between the austenitic matrix and precipitates can be established: $<100>_P//\ <100>_a$.

3.5. Magnetic properties

The Curie temperatures of the samples were about $T_C=(370\pm5)$ K, relatively close to those reported for Ni_2MnGa bulk samples [35,36].

Room temperature magnetic hysteresis curves were measured up to 1.5 T, at a field rate of 0.75 T/min. The samples are all ferromagnetic and the hysteresis J vs. $\mu_0 H_i$ curves of the austenitic phase are presented in Fig. 9; the corresponding values of the saturation (J_S) and remanent (J_R) polarizations, and the coercive field $\mu_0 {}_J H_{ic}$, defined as the internal field at which $J=0$, are listed in Table 2. The coercivity and polarization values measured in V10 and V15 are relatively close to those reported in arc melt polycrystalline Ni_2MnGa austenitic alloys [38]; on the other hand, the saturation polarization of V20 is somewhat smaller, in agreement with results indicating that high quenching rates promote local disorder which lowers the spontaneous polarization values in the austenitic phase [38]. In fact, the Mn atoms at Ga sites (the nearest neighbors of Mn in the ordered state) couple antiferromagnetically to the dominant moment leading to a lower polarization.

The room temperature major loops are well fitted by a soft ferromagnetic contribution and a small linear contribution, probably arising from the small Mn(S,Se) precipitates; it is known that MnS and MnSe phases transform from paramagnetic to antiferromagnetic at $T_N \approx 150$ K [39].

The magnetic polarization versus temperature is investigated in the range 4–300 K, where the martensitic transformation is expected to take place; measurements are performed in all the samples in both, the zero field cooled (ZFC) and the field cooled (FC) magnetic states. Each sample was first cooled from room temperature to 4 K, without any applied field, and the polarization was recorded during heating under an applied field of 2 mT (ZFC). Then the polarization was measured during the subsequent cooling and heating (FC curve), keeping the applied field constant. The resulting curves are shown in Fig. 10 a–c. Curve a' corresponds to a thermal cycle performed in sample V10 but with an applied field of 0.5 T.

During cooling from 300 K the magnetic polarization of all the samples undergoes a sharp decrease; during the subsequent heating the polarization practically recovers at a higher temperature leading to a relatively large hysteresis. The total polarization changes associated with the transformation under a small applied field of 2 mT are about 16 mT (V10), 1.3 mT (V15) and 1.1 mT (V20). For sample V10 transforming in a larger magnetic field of

Table 2
Room temperature hysteresis parameters for the austenitic phase: saturation polarization J_S remanent polarization J_R and coercive field $\mu_0 {}_J H_{ic}$ at which $J=0$.

Sample	V10	V15	V20
J_S [T]	0.6618	0.6550	0.4793
J_R [T]	0.0661	0.034	0.0235
$\mu_0 {}_J H_{ic}$ [mT]	5.2	4.5	3.6

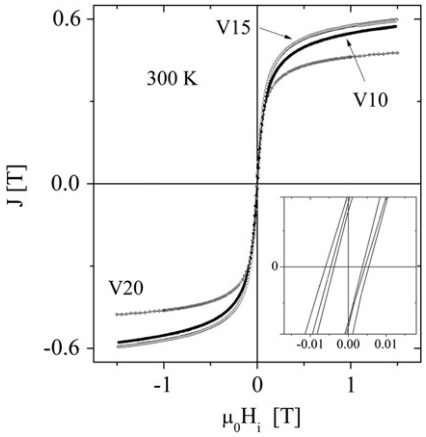

Fig. 9. Room temperature hysteresis loops corresponding to the samples in austenitic phase. These loops are well fitted by a soft ferromagnetic contribution and a paramagnetic one, probably arising from the Mn(S,Se) precipitates.

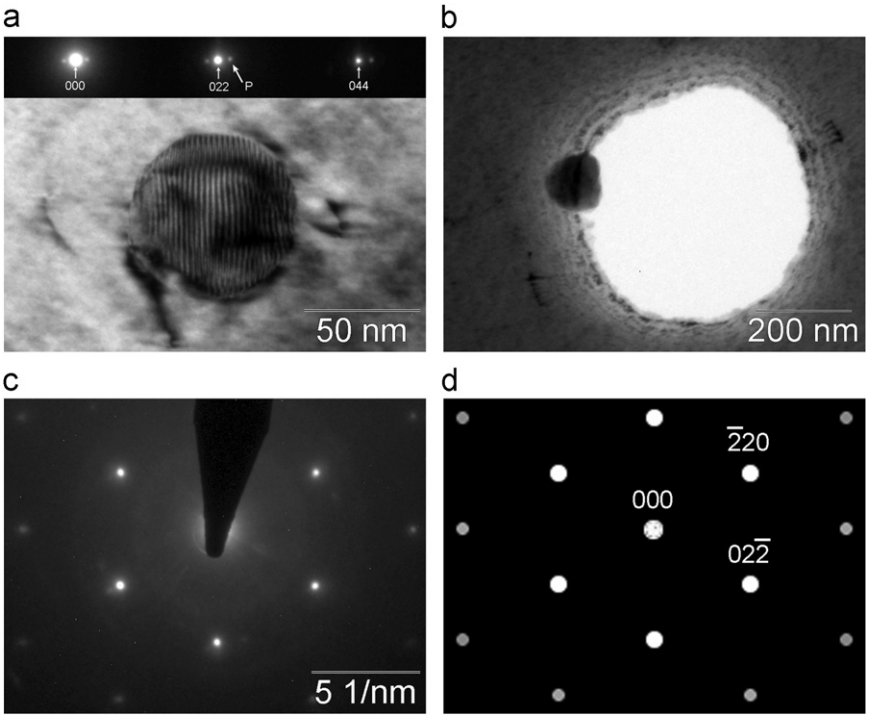

Fig. 8. (a) Precipitate (70 nm diameter) in sample V10 exhibiting Moiré fringes. The upper side of the image presents the corresponding electron diffraction pattern showing austenite and precipitate (P) spots. Non indexed reflections correspond to double diffraction. (b) Precipitate (110 nm) located at the edge of a hole in sample V15. (c) Selected area electron diffraction pattern of the precipitate in (b). (d) Simulation of the [1 1 1] zone axis pattern corresponding to MnSe (Na–Cl-type structure). This pattern matches the experimental one suggesting a similar structure for the precipitates.

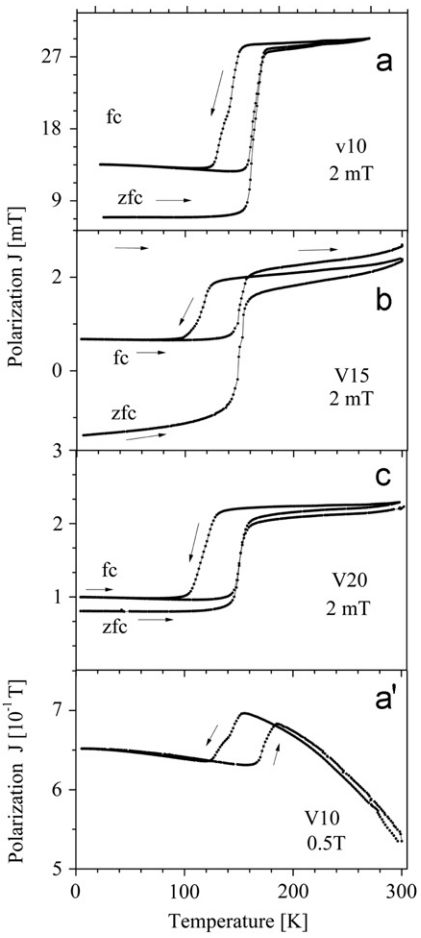

Fig. 10. Magnetization vs. temperature curves in the ZFC and FC conditions, measured under a constant field of 2 mT in samples V10 (a), V15 (b) and V20 (c) and under a field of 0.5 T in V10 (a'). The steps in the curves are attributed to the martensitic transformation.

Table 3
Temperatures corresponding to the martensitic T_M and the austenitic T_A transformations in samples Ni_2MnGa, solidified by twin roller melt spinning at tangential wheel speeds of 10 m/s (V10), 15 m/s (V15) and 20 m/s (V20). The transformation onset temperatures T_{MR}, T_{AR} and T_I observed in the electrical resistance vs. temperature curves shown in Fig. 11 are also included. $\mu_0 H_A$ is the constant field applied during the magnetization vs. temperature measurements.

Sample	T_M [K]	T_A [K]	T_{MR} [K]	T_{AR} [K]	T_I [K]
V10	149	170	126	163	228
	148[a]	168[a]			
V15	119	150	123	146	231
V20	118	150	129	144	217

[a] $\mu_0 H_A$= 0.5 T.

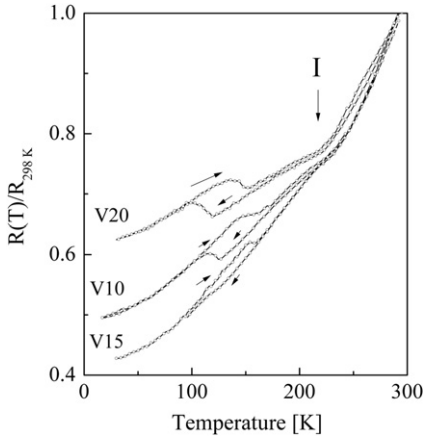

Fig. 11. Electrical resistance vs. temperature curves showing the intermediate transformation temperature T_I and the martensitic transformation temperatures for the samples investigated.

0.5 T this change is about 58.5 mT. The para- to antiferromagnetic transformation of the Mn(Se,S) precipitates at T_N= 150K cannot explain this hysteretic behavior. On contrary, the phase transformation reported in this alloy from the high temperature austenitic phase (A) to a martensitic phase (M) during cooling (T_M) and the re-transformation $M \rightarrow A$ (T_A) during heating would explain both, the polarization changes and hysteresis. The martensitic transformation temperature is not affected by the magnitude of the applied field during measuring, as illustrated in Figs. 10a and a′.

The low anisotropy energy of the austenitic cubic phase makes it magnetically soft, with low coercivity and remanence, and also little hysteresis. On the other hand, martensite exhibits a relatively large uniaxial anisotropy. These facts allow the martensitic transformation to be observed by field cooling the material through the transition temperature. A significant drop in the magnetic moment is observed as the transformation proceeds as a consequence of an increased magnetic anisotropy and a reduction in the number of easy magnetization axes aligned close to the applied field direction [6,35].

The transformation temperatures T_M and T_A, estimated as those where the curves (dJ/dT) exhibit a local maximum, are listed in Table 3 together with the transformation temperatures corresponding to *the onset* of the martensitic T_{MR} and austenitic T_{AR} transformations determined by the resistance vs. temperature measurements shown in Fig. 11. A good agreement is found between these values but they are lower than those measured in bulk Ni_2MnGa alloys (T_M=202 K) [35]. The decrease observed in the martensitic transformation temperature can be correlated to grain size. Melt-spun ribbons with grain refinement have a larger amount of grain boundaries, in which the short-range atomic chemical disorder is increased. This disorder enhances the resistance to the transformation and lowers the martensitic transformation temperature [40].

A new transition is detected by resistivity measurements, around 230 K, which is identified as that leading to an intermediate, premartensitic phase. During cooling Ni_2MnGa single crystals, the reported transformation sequence is [41–44]: $A \rightarrow I \rightarrow 10M$, where A is the austenitic phase, I an intermediate (premartensitic) phase and 10 M a martensitic phase. In fact, Ni_2MnGa alloys exhibit, during cooling, a soft-mode-condensed premartensitic transition to a cubic I phase and then another transition to a tetragonal 10 M modulated martensite [45]. On the other hand, in polycrystalline $Ni_{51}Mn_{28.5}Ga_{20.5}$ ribbons processed by single-roller melt spinning, a transition from a high temperature cubic austenitic phase to a 7 M or 14 M orthorhombic martensite is reported during cooling [25,46]. It is often found that austenite transforms to a mixture of layered structures, with overlapping stability ranges and/or they show a different sequence on cooling and heating; also, internal stresses may promote different inter-martensitic transformations [47] leading to different final low temperature products. These facts make the identification of the low temperature martensitic phase difficult; unfortunately, we could not access to low temperature X ray or neutron diffraction nor to TEM facilities to characterize the martensitic phase.

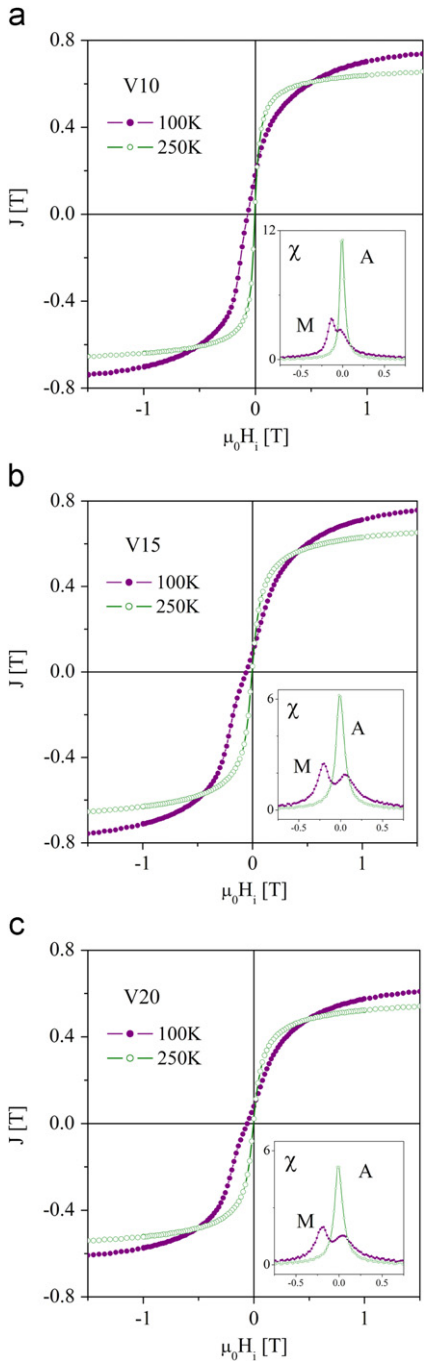

Fig. 12. Upper branch of the hysteresis loops measured at 100 K and 250 K for samples V10 (a), V15 (b) and V20 (c). The loops corresponding to the samples in the martensitic phase show two steps, as illustrated by the χ curves in the insets.

The upper branch of the isothermal hysteresis loops measured at different temperatures and the differential susceptibility χ curves for two temperatures – one in the range of the austenitic high temperature phase and another one at low temperature, where the transformation is complete – are shown in Fig. 12 for the three microstructures investigated. It is worth to note that *two* distinct peaks are detected during demagnetization of the martensitic phase from saturation; the first maximum in the $\chi(H)$ plot (first step in the demagnetization curve) of samples V15 and V20 appears at a positive (first quadrant) internal field (about 46 mT) while in sample V10 it is located at a small inverse field (-25 mT). For increasing demagnetizing inverse fields, another step is observed at about -128 mT (V10) and -235 mT (V15 and V20). These features of the hysteresis loop are completely reproduced during subsequent field cycles. The larger step has already been observed in $Ni_{51}Mn_{28.5}Ga_{20.5}$ polycrystalline ribbons, processed by single roller melt spinning [25,46], and they were attributed to magnetic field induced twin boundary motion (MFITBM) in the martensitic phase. The authors explain the phenomenon on the basis of the ribbon crystallographic texture and the internal stresses built up during quenching [25,46] which induce the cubic austenite to transform into orthorhombic martensite during cooling. This quenched tensile stresses promote those twin variants with hard magnetization

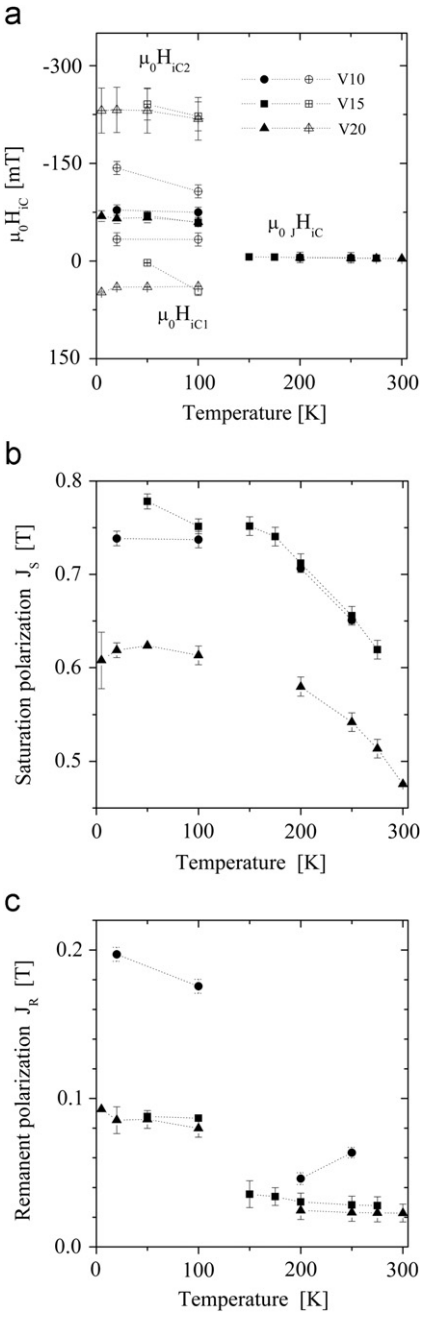

Fig. 13. Coercive field (a), saturation polarization (b) and remanent polarization (c) as functions of temperature for the alloys investigated. In (a), the coercive field $\mu_0 {}_J H_{ic}$ at which $J=0$, is denoted with full symbols, while the critical fields associated to the steps observed in the demagnetization curves of the martensitic phase (Fig. 12, insets) are indicated with open symbols.

direction – *a* axis – parallel to the stress direction (ribbon plane) and the shortest *c* (easy) axis of the orthorhombic lattice normally aligned with the stress. The abrupt slope change in the martensite $J(H)$ curves would correspond to the onset of MFITBM in the preferentially oriented martensite. The restoring 'force' leading to reversible twin boundary motion is proposed to be the grain-to-grain elastic energy stored in the polycrystalline ribbon. Even when similar texture and quenched-in stresses are also present in our samples, it is not possible to confirm that the same mechanisms are responsible for the large peak in the $\chi(H)$ curves at $\mu_0\ {}_{\chi}H_{ic2}$ because the nature of the martensitic phase remains unknown. The same arguments apply to the small peak in $\chi(H)$ at $\mu_0\ {}_{\chi}H_{ic1}$, not reported for single roller melt spun samples.

Fig. 13 summarizes the temperature dependence of the hysteresis parameters for samples V10, V15 and V20. The coercive field $\mu_0\ {}_{J}H_{ic}$ is plotted together with the two critical fields defined as the internal fields at which the curve $\chi(T)$ reaches local maxima, $\mu_0\ {}_{\chi}H_{ic1}$ and $\mu_0\ {}_{\chi}H_{ic2}$, respectively.

4. Summary

Stoichiometric Ni_2MnGa thin ribbons (40 μm thick) were produced by twin roller melt spinning at three different cooling rates to explore the effects of this symmetric, ultra fast quenching condition on the alloy microstructure and magnetic properties.

Samples are polycrystalline, with small (4 μm) equiaxed grains near the surfaces and columnar grains 2–6 μm in diameter and 10–20 μm length, developed along the main heat extraction direction. These columnar grains are longer and thicker in samples cooled at lower rates. The samples exhibit a large crystallographic texture with the [400] direction perpendicular to the ribbon plane, which becomes more marked in samples quenched at higher rates.

The equilibrium major phase at room temperature is the cubic $L2_1$ Ni_2MnGa ordered austenitic phase in all the samples, with a lattice parameter only ~0.1% larger than the tabulated value. The mean size of the order domains changes from 40 nm to about 19 nm when the substrate speed changes from 10 m/s to 20 m/s. Mn (S,Se) precipitates are also observed embedded in the matrix, with mean particle size and density increasing as the quenching rate decreases; these precipitates keep a definite orientation relation with the matrix, $<100>_P // <100>_a$. The austenitic matrix is ferromagnetic and the precipitates are paramagnetic above 150 K. Together with the antiphase boundaries between order domains, these precipitates are expected to hinder domain wall motion in the matrix; however, all samples in the austenitic phase exhibit very low coercivities, near 3–6 mT.

Magnetic polarization and electrical resistance vs. temperature measurements performed in samples in the as-cast condition indicate that the alloys transform to an intermediate cubic phase I at about 220–230 K depending on the quenching rate and to a martensitic phase at about 130 K. This martensite is also ferromagnetic and the $J(H)$ loops exhibit larger coercivity and remanence values than those measured in the austenitic phase. The low temperature hysteresis loops, corresponding to the martensitic phase, show similar features as those reported by other authors in melt spun Ni–Mn–Ga ribbons. The demagnetization curves measured from saturation in the martensitic state show two marked steps: a first one for positive fields in V15 and V10 (~46 mT) and a larger second one for relatively large inverse fields (~130–250 mT) in all the samples. These steps are likely to arise from a demagnetization mechanism involving field induced twin boundary motion in the few martensite variants selected by the crystallographic texture and the stresses built up in the ribbons during quenching.

Acknowledgments

The authors thank CONICET, ANPCyT, SECyT-UNC and SECyT-UNCu for the financial support given to this work. The authors also thank to Mr. Carlos Cotaro for his help in SEM measurements.

References

[1] K. Ullakko, J.K. Huang, C. Kantner, R.C. O'Handley, V.V. Kokorin, Large magnetic-field-induced strains in Ni_2MnGa single crystals, Applied Physics Letters 69 (13) (1996) 1966–1968.
[2] A. Sozinov, A.A. Likhachev, N. Lanska, K. Ullakko, Giant magnetic-field-induced strain in NiMnGa seven-layered martensitic phase, Applied Physics Letters 80 (10) (2002) 1746–1748.
[3] A.N. Vasil'ev, A.D. Bozhko, V.V. Khovailo, I.E. Dikshtein, V.G. Shavrov, V.D. Buchelnikov, M. Matsumoto, S. Suzuki, T. Takagi, J. Tani, Structural and magnetic phase transitions in shape-memory alloys $Ni_{2+x}Mn_{1-x}Ga$, Physical Review B 59 (2) (1999) 1113–1120.
[4] R. Kainuma, Y. Imano, W. Ito, Y. Sutou, H. Morito, S. Okamoto, O. Kitakami, K. Oikawa, A. Fujita, T. Kanomata, K. Ishida, Nature (London) 439 (2006) 957–960.
[5] D.C. Dunand, P. Müllner, Size effects on magnetic actuation in Ni-Mn-Ga shape-memory alloy, Advanced Materials 23 (2011) 216–232.
[6] O. Söderberg, A. Sozinov, Y. Ge, S.-P. Hannula, V.K. Lindroos, Giant magnetostrictive materials, in: K.H.J. Buschow (Ed.), Handbook of Magnetic Materials, vol. 16, Elsevier Science, Amsterdam, 2005.
[7] R.C. O'Handley, S.M. Allen, Shape memory alloys, magnetically activated ferromagnetic shape memory materials in M Schwartz, Encyclopedia of Smart Materials, Wiley, New York, 2001 936–951.
[8] A. Vassil'ev, Magnetic driven shape memory alloys, Journal of Magnetism and Magnetic Materials 242–245 (2002) 66–67.
[9] B. Jiang, W. Zhou, Y. Liu, X. Qi, Recent progress of magnetically controlled shape memory materials, Materials Science Forum 426–432 (2003) 2285–2290.
[10] O. Heczko, Magnetic shape memory effect and magnetization reversal, Journal of Magnetism and Magnetic Materials 290–291 (2005) 787–794.
[11] J. Enkovaara, A. Ayuela, T. Zayak, P. Entel, L. Nordström, M. Dube, J. Jalkanen, J. Impola, R.M. Nieminen, Magnetically driven shape memory alloys, Materials Science and Engineering A 378 (2004) 52–60.
[12] S.J. Murray, M. Marioni, S.M. Allen, R.C. O'Handley, T.A. Lograsso, Appl. Phys. Lett. **77** (2000) 886–888.
[13] P. Müllner, V.A. Chernenko, M. Wollgarten, G. Kostorz, Large cyclic deformation of a Ni-Mn-Ga shape memory alloy induced by magnetic fields, Journal of Applied Physics 92 (2002) 6708–6713.
[14] M. Thomas, O. Heczko, J. Buschbeck, L. Schultz, S. Fähler, Stress induced martensite in epitaxial Ni–Mn–Ga films deposited on MgO(001), Applied Physics Letters 92 (2008) 192515–192517.
[15] G.J. Mahnke, M. Seibt, S.G. Mayr, Microstructure and twinning in epitaxial NiMnGa films, Physical Review B 78 (2008) 012101.
[16] O. Heczko, M. Thomas, J. Buschbeck, L. Schultz, S. Fähler, Epitaxial Ni–Mn–Ga films deposited on SrTiO3 and evidence of magnetically induced reorientation of martensitic variants at room temperature, Applied Physics Letters 92 (2008) 072502-4'.
[17] Y. Boonyongmaneerat, M. Chmielus, D.C. Dunand, P. Müllner, Increasing magnetoplasticity in polycrystalline Ni-Mn-Ga by reducing internal constraints through porosity, Physical Review Letters 99 (2007) 247201–247204.
[18] Y.J. Tang, D.J. Smith, H. Hu, F.E. Spada, H. Harper, A.E. Berkowitz, Structure and phase transformation of ferromagnetic shape memory alloy $Ni_{49}Mn_{30}Ga_{21}$ fine particles prepared by spark erosion, IEEE Transactions on Magnetics 39 (5) (2003) 3405–3407.
[19] V.A. Chernenko, G.N. Kakazeia, A.O. Perekos, E. Cesari, S. Besseghini, Magnetization anomalies in melt-spun Ni–Mn–Ga ribbons, Journal of Magnetism and Magnetic Materials 320 (2008) 1063–1067.
[20] Z.H. Liu, J.L. Chen, H.N. Hu, M. Zhang, X.F. Dai, Z.Y. Zhu, G.D. Liu, G.H. Wu, F.B. Meng, Y.X. Li, The influence of heat treatment on the magnetic and phase transformation properties of quaternary Heusler alloy $Ni_{50}Mn_8Fe_{17}Ga_{25}$ ribbons, Scripta Materialia 51 (2004) 1011–1015.
[21] F. Albertini, S. Besseghini, A. Paoluzi, L. Pareti, M. Pasquale, F. Passaretti, C.P. Sasso, A. Stantero, E. Villa, Structural, magnetic and anisotropic properties of Ni_2MnGa melt-spun ribbons, Journal of Magnetism and Magnetic Materials 242–245 (2002) 1421–1424.
[22] T. Goryczka, J. Lelatko, B. Gorka-Kostrubiec, P. Ochin, H. Morawiec, Martensitic transformation in melt-spun Ni-Mn-Ga ribbons', European Physical Journal - Special Topics 158 (2008) 131–136.
[23] N. Dearing, A.G. Jenner, Magnetic and magnetoelastic properties of melt-spun Ni-Mn-Ga, IEEE Transactions on Magnetics 42 (2006) 78–80.
[24] J. Gutierrez, J.M. Barandiaran, P. Lazpita, C. Segui, E. Cesari, Magnetic properties of a rapidly quenched Ni–Mn–Ga shape memory alloy, Sensors and Actuators A 129 (2006) 163–166.
[25] J. Wang, C. Jiang, R. Techapiesancharoenkij, D. Bono, S.M. Allen, R.C. O'Handley, Anomalous magnetizations in melt spinning Ni–Mn–Ga, Journal of Applied Physics 106 (2009) 023923-1-3.

[26] R.C. O'Handley, S.J. Murray, M. Marioni, H. Nembach, S.M. Allen, Phenomenology of giant magnetic-field-induced strain in ferromagnetic shape-memory materials, Journal of Applied Physics 87 (9) (2000) 4712–4717.
[27] Amikam Aharoni, Demagnetizing factors for rectangular ferromagnetic prisms, Journal of Applied Physics 83 (1998) 3432–3434.
[28] Werner Scholz – Parallel Finite Element Micromagnetics Package-Magpar-Copyright (C) 2002–2010.
[29] I. Babita, M. Manivel Raja, R. Gopalan, V. Chandrasekaran, S. Ram, Phase transformation and magnetic properties in Ni–Mn–Ga Heusler alloys, J. of Alloys and Compounds 432 (2007) 23–29.
[30] Y. Takamura, R. Nakane, S. Sugahara, Analysis of $L2_1$-ordering in full-Heusler Co_2FeSi alloy thin films formed by rapid thermal annealing, Journal of Applied Physics 105 (2009) 07B109.
[31] H. Klug, L. Alexander, X-ray Diffraction Procedures for Polycrystalline and Amorphous Materials, 2nd ed., John Wiley and Sons, New York, 1974, p. 687.
[32] S. Vives, E. Gaffet, C. Meunier, X-ray diffraction line profile analysis of iron ball milled powders, Materials Science and Engineering A 366 (2004) 229–238.
[33] C. Dong, F. Wu, H. Chen, Correction of zero shift in powder diffraction patterns using the reflection-pair method, Journal of Applied Crystallography 32 (1999) 850–853.
[34] Y. Ma, S. Awaji, K. Watanabe, M. Matsumoto, N. Kobayashi, X-ray diffraction study of the structural phase transition of Ni_2MnGa alloys in high magnetic fields, Solid State Communications 113 (2000) 671–676.
[35] P.J. Webster, K.R.A. Ziebeck, S.L. Town, M.S. Peak, Magnetic Order and Phase Transformation in Ni_2MnGa, Philosophical Magazine Part B 49 (1984) 295–310.
[36] C. Jiang, Y. Muhammad, L. Deng, W. Wu, H. Xu, Composition dependence on the martensitic structures of the Mn-rich NiMnGa alloys, Acta Materialia 52 (2004) 2779–2785.
[37] G.D. Serrano, J.L. Pelegrina, A.M. Condó, M. Ahlers, Helical dislocations as vacancy sinks in β phase Cu–Zn–Al–Ni alloys, Materials Science and Engineering A 433 (2006) 149–154.
[38] C. Seguí, J. Pons, E. Cesari, Effect of atomic ordering on the phase transformations in Ni–Mn–Ga shape memory alloys, Acta Materialia 55 (2007) 1649–1655.
[39] Binary alloy phase diagrams, Editor-in-chief: Massalski, T. B.; in: Okamoto, H. Subramanian, P.R. Kacprzak, L. (Eds.) 2nd ed. ASM International, Materials Park, Ohio, 1990.
[40] S. Guo, Y. Zhang, J. Li, B. Quan, Y. Qi, X. Wang, Martensitic transformation and magnetic-field-induced strain in magnetic shape memory alloy NiMnGa melt-spun ribbon, Journal of Materials Science & Technology 21 (2005) 211–214.
[41] J. Kim, F. Inaba, T. Fukuda, T. Kakeshita, Effect of magnetic field on martensitic transformation temperature in Ni–Mn–Ga ferromagnetic shape memory alloys, Acta Materialia 54 (2006) 493–499.
[42] V.A. Chernenko, E. Cesari, V.V. Kokorin, I.N. Vitenko, The development of new ferromagnetic shape memory alloys in Ni-Mn-Ga system, Scripta Materialia 33 (1995) 1239–1244.
[43] J. Pons, V.A. Chernenko, R. Santamarta, E. Cesari, Crystal structure of martensitic phases in Ni–Mn–Ga shape memory alloys, Acta Materialia 48 (2000) 3027–3038.
[44] B. Wedel, M. Suzuki, Y. Murakami, C. Wedel, T. Suzuki, D. Shindo, K. Itagaki, Low temperature crystal structure of Ni–Mn–Ga alloys, Journal of Alloys and Compounds 290 (1999) 137–142.
[45] A. Zheludev, S.M. Shapiro, P. Wochner, A. Schwartz, M. Wall, L.E. Tanner, Phonon anomaly, central peak, and microstructures in Ni_2MnGa, Physical Review B 51 (1995) 11310–11314.
[46] J. Wang, C. Jiang, R. Techapiesancharoenkij, David Bono, S.M. Allen, R.C. O'Handley, Microstructure and magnetic properties of melt spinning Ni- Mn-Ga, Intermetallics 32 (2013) 151–155.
[47] E. Cesari, V.A. Chernenko, V.V. Kokorin, J. Pons, C. Seguı, Internal friction associated with the structural phase transformations in Ni-Mn-Ga alloys, Acta Materialia 45 (1997) 999–1004.